

N71-24146

NASA TECHNICAL
MEMORANDUM

NASA TM X-62-019

NASA TM X-62,019

**CASE FILE
COPY**

LUNAR ELECTRICAL CONDUCTIVITY FROM APOLLO 12
MAGNETOMETER MEASUREMENTS:
COMPOSITIONAL AND THERMAL INFERENCES

C. P. Sonett, G. Schubert, B. F. Smith, K. Schwartz, and D. S. Colburn

Ames Research Center
Moffett Field, Calif. 94035

April 1971

Lunar Electrical Conductivity
from Apollo 12 Magnetometer Measurements:
Compositional and Thermal Inferences

C.P. SONETT, G. SCHUBERT^{*}, B.F. SMITH^{*},
K. SCHWARTZ[†], and D.S. COLBURN

NASA Ames Research Center
Moffett Field, California 94035

^{*} University of California, Los Angeles, California 90024

[†] American Nucleonics Corp., Woodland Hills, California 91364

To appear in Proc. Apollo 12 Lunar Science Conf., Geochim.
Cosmochim. Acta. Suppl.

ABSTRACT

The lunar electrical conductivity profile has been obtained from an iterative fit of theoretical electromagnetic transfer functions to empirical ones based on joint power spectral density analyses of data from the Apollo 12 Lunar Surface Magnetometer and the Ames Explorer 35 magnetometer. Seven selected two hour swaths and seven selected one hour swaths of data were used. The spectrum analyzed ranged in frequency from 0.00083 to 0.04 Hz. The amplification of the interplanetary magnetic field at the lunar surface showed a distinct increase from ~ 1 at 0.001 Hz to ~ 3 at 0.005 Hz. At higher frequencies the slope of the amplification vs. frequency curve decreases until the amplification levels off at about 4 at 0.025 Hz. An amplification curve with such a distinct bend is best fit by a lunar conductivity model with a sharp maximum around 1500 km radius, so that high frequency variations in the magnetic field are compressed into the outer shell while low frequency variations can penetrate to the interior. For a monotonic temperature profile, the electrical conductivity model requires a change in composition around 1450 km radius. A thermal and compositional model which appears to fit the data is a basalt-like outer layer, an olivine-like core and a temperature of 450°C at the conductivity peak, increasing to 800°C in the deep core.

INTRODUCTION

This paper extends our preliminary report (SONETT et al., 1971a) of the bulk electrical conductivity profile of the Moon determined by analysis of data from the Apollo 12 Lunar Surface Magnetometer (LSM) and the Ames Explorer 35 lunar orbiter magnetometer. The account given here is still exploratory but more details are supplied on the mechanism of induction, the analysis, and the implications of our findings.

It has been recognized in recent years that electromagnetic excitation of the Moon by signals arising in the solar wind produce electrical currents in the deep lunar interior. The magnetic fields associated with these currents are detectable at the surface of the Moon (SONETT et al., 1971a, b,c; DYAL et al., 1970) and, in the case of a strong inductive response may even modify the plasma flow near the Moon. The establishment of Explorer 35 in lunar orbit permitted study of the plasma environment close to the Moon. However, the detection of electromagnetic events in the Moon appears to be feasible only from either the surface or a very low altitude orbiter. Using the LSM, lunar electromagnetic induction can be assured. We believe the corresponding theory is sufficiently well understood that lunar magnetometry can be used to determine the electrical conductivity of the interior and thence to make inferences of temperature and composition. Although a detailed

analysis of spatial resolution has so far not been carried out, our preliminary assessment is that volume elements of the order of 3% are resolvable in the region of the steep conductivity rise with depth.

A fundamental difference of the Moon from the earth arises from the solar wind. When the angle between the Moon-sun line and the local vertical at the LSM is appreciably less than 90° , the dynamic pressure of the solar wind is known to compress the induced magnetic field into the less conducting subsurface layers of the Moon (SONETT et al., 1971a), appreciably amplifying the induction over that in a pure vacuum or a nonconducting atmosphere. This distinction together with the presence of the diamagnetic cavity results in a day-night induction asymmetry.

MECHANISM OF THE INDUCTION

Electromagnetic induction in the Moon is dependent upon a variety of discontinuities and waves in the solar wind. The forcing function which drives the induction is composed of the steady interplanetary magnetic field upon which is superimposed a hydromagnetic radiation continuum due to (1) plasma waves arising presumably in the solar atmosphere and subsequently convected and propagated outwards, (2) waves due to local instabilities in the solar wind, and (3) discrete large amplitude events such as collision-free shock waves, tangential dis-

continuities, and Alfvén waves (cf. COLBURN and SONETT, 1966^{*}).

The electromagnetic interaction includes toroidal and poloidal magnetic fields. The principle excitations for these are a) the interplanetary electric field (in a reference frame comoving with the Moon) given by $\underline{E}_m = \underline{v} \times \underline{B}$, where \underline{v} is the velocity of the Moon relative to the solar wind and \underline{B} the instantaneous interplanetary magnetic field, and b) the time rate of change of the interplanetary field, $\dot{\underline{B}}$. The two modes correspond respectively to transverse magnetic (TM) and transverse electric (TE) excitation. Both modes display strong frequency (f) dependence. The TE transfer function is zero at $f = 0$ and increases with increasing f . The TE mode currents which close wholly in the lunar interior, tend to be concentrated where variations in the magnetic field are damped substantially. With increasing frequency, the poloidal fields become compressed into shells of decreasing thickness, thus increasing the amplification of the magnetic field as observed at the Moon's surface. Examination of the interior of the Moon to depths around 800 km is facilitated by this mode, but for greater depths is limited by the decreased response.

The TM mode attains peak value for $f = 0$; it remains approximately constant with increasing f until a combination of core and lithospheric conductivities forces the currents to

* Although a large body of experimental work has subsequently been published, this paper provides the essential background for large events.

pass wholly through the crust whereupon it decreases with further increase in f beyond about 0.03 Hz. This mode is responsible for steady state bow wave phenomena. Attempts to detect a bow wave in the solar wind upstream from the Moon have not met with success. The TM current system, which is required to pass through the lunar crust and close in the solar wind, is consequently limited to less than 10^5 amperes. However, as shown later, the total absence of the TM mode is not assured and evidence for this mode is present.

Theoretical treatments of the lunar interaction with the solar wind generally include the effect of the solar wind dynamic pressure in confining the induced field lines (SONETT and COLBURN, 1968; JOHNSON and MIDGLEY, 1968; BLANK and SILL, 1969; SCHUBERT and SCHWARTZ, 1969). This effect is provided in the model by a field confining surface current layer in the solar wind just ahead of the lunar surface. Preliminary examination of the lunar response using the LSM data shows a strong amplification of incident tangential discontinuities whose free stream properties are monitored by Explorer 35. The amplification occurs only for the vector components tangential to the surface; the normal component tends to follow the interplanetary value. Thus the existence of a confining current layer appears verified for the sunward side of the Moon. The very strong amplification implies that the lines of force

are confined within the Moon to a crustal layer having an electrical conductivity substantially less than that of the deeper layers(SONETT et al., 1971b).

THEORY OF THE INDUCTION

A complete treatment of the electromagnetic interaction would require appropriate matching of the interior fields to those in the plasma surrounding the Moon. The exterior flow field shows no marked perturbations aside from the diamagnetic cavity. An analysis based upon an inhomogeneous Moon immersed within a perfectly conducting space is used for the sunward hemisphere. This simplification is justified since cavity current effects are much smaller on the sunward hemisphere.

We consider the interaction of a solar wind forcing magnetic field oscillation

$$\underline{H} = \hat{\eta} H_0 \exp\left\{2\pi i \left(\frac{\zeta}{\lambda} - ft\right)\right\}, \quad (1)$$

with a radially inhomogeneous Moon. The cartesian coordinate system (ξ, η, ζ) with unit vectors $\hat{\xi}, \hat{\eta}, \hat{\zeta}$ is fixed relative to the Moon and has its origin at the Moon's center. The Moon moves with speed v in the negative ζ direction. The quantities H_0 and $\lambda = v/f$ are the amplitude and wavelength, respectively, of the magnetic field oscillation. The magnetic

field forcing function alone drives the TE lunar response. A derivation for the TM mode response is not included here because it must be relatively unimportant (see the discussion in the following section). In the lunar interior the solution of Maxwell's equations for the TE mode can be represented by the potential Ω which satisfies

$$\nabla^2 \Omega + k^2 \Omega = 0 \quad , \quad (2)$$

where

$$k^2 = \omega^2 \mu \epsilon + i \sigma \mu \omega \quad , \quad \omega = 2\pi f \quad , \quad (3)$$

σ is the electrical conductivity, and μ and ϵ are respectively the magnetic permeability and permittivity of the Moon. Although some possibility exists that local effects are significant in increasing the value of μ over the free space value, there is presently no evidence for this. DYAL and PARKIN (1971) give $(1.03 \pm 0.03)\mu_0$ for the global permeability. In the following discussion the values assumed for the global permeability and permittivity of the Moon are the free space values of these quantities. Possible departures of the permittivity from the free space value are insignificant in the subsequent application of this theory. The equations for determining \underline{H} from the potential

Ω are presented in the Appendix.

The boundary condition applied to the TE mode is the continuity of the normal component of the magnetic field at the lunar surface. This condition results from the confinement of the induced field, treated as a current sheet at the Moon-plasma interface.

The potential Ω is given by

$$\Omega = \mu v H_0 \frac{a}{r} \sin \varphi \sum_{\ell=1}^{\infty} \beta_{\ell} G_{\ell}(r) P_{\ell}^1(\cos \theta) \quad , \quad (4)$$

where (r, θ, φ) are spherical polar coordinates with ζ the polar axis, a is the lunar radius, β_{ℓ} is $\frac{i^{\ell}(2\ell+1)}{\ell(\ell+1)}$, and P_{ℓ}^1 are associated Legendre polynomials. The functions G_{ℓ} are solutions of

$$\frac{d^2 G_{\ell}}{dr^2} + \left\{ k^2 - \frac{\ell(\ell+1)}{r^2} \right\} G_{\ell} = 0 \quad , \quad (5)$$

with the boundary conditions

$$G_{\ell}(r=a) = j_{\ell} \left(\frac{2\pi a}{\lambda} \right) \quad , \quad (6)$$

where j_{ℓ} are the spherical Bessel functions. The equation for the potential and the form of the boundary conditions

follow, in part, from the character of the spherical harmonic expansion of the solar wind forcing field, given in the Appendix. LAHIRI and PRICE (1939) were the first to obtain the radial differential equation for the TE mode in connection with their investigation of the geomagnetic induction problem.

For the interpretation of LSM data we introduce the modal transfer function for the tangential components of the TE mode magnetic field at the lunar surface

$$\frac{a \frac{dG_{\ell}}{dr}}{\frac{d}{da} \left\{ a j_{\ell} \left(\frac{2\pi a}{\lambda} \right) \right\}} \quad (\text{see Appendix})$$

INSTRUMENTATION AND DATA

General properties of both the LSM and the Ames magnetometer on Explorer 35 are given elsewhere (DYAL et al., 1970; MIHALOV et al., 1968). Provision has been made in the Explorer magnetometer for the suppression of spin tone modulation of the data spectrum by utilizing a pair of synchronous demodulators which operate in quadrature upon the two spin tone modulated signals. This suppression is done on the spacecraft and can be shown to lead to a time series from which spin modulation is ideally eliminated. The signals returned to Earth are formally identical to those obtained from a nonspinning inertially stable

spacecraft (SONETT, 1966).

A sample and hold system samples the three components of the vector at a uniform rate. In order to avoid the risk of unacceptable alias the magnetometer outputs are passed through a low pass filter prior to sampling, according to the Nyquist criterion. The effect of filter rolloff is significant for frequencies above 0.025 Hz, which is the 3 db point. The power spectral densities have been corrected for this effect at all frequencies.

Spectra have been obtained both for cases where the Moon is in the magnetosheath and also in the free stream solar wind. The forcing field defined by Explorer 35 measurements is transformed into the local LSM coordinate system (x is along the normal outwards from the surface, y is easterly and z is northerly at the site of ALSEP and the LSM). The LSM data, which define the response field, are edited to eliminate spurious data and to insure time continuity. Time gaps and noise in the LSM data are aperiodic and are attributed to telemetry transmission and data processing. For the cases studied the amount of data missing or deleted because of gaps and spurious noise is small (< 5%). The data are then numerically filtered and decimated in order to analyze segments of the record with approximately the same sampling interval and upper frequency

limit as that from Explorer 35, the latter having a Nyquist limit approximately one order less than LSM. The Explorer data are similarly edited to insure time continuity and to remove obvious spurious signals. For the Explorer data the time series are continuous for the intervals studied. Spurious signals at random intervals, are removed and again constitute a small amount of the time interval ($< 5\%$).

The power spectral densities for the forcing and response fields are computed using standard techniques for determining the autocorrelation function, smoothing, and taking the Fourier transform (BENDAT and PIERSOL, 1966; JENKINS and WATTS, 1968). The spectra are analyzed using 20 degrees of freedom, and the autocorrelation function is smoothed with a Parzen weighting function (JENKINS and WATTS, 1968). This gives an approximate error of 25 per cent in each power spectral density estimate. We have applied these techniques to seven selected two hour swaths and seven selected one hour swaths of data. Longer swaths, which would have reduced the horizontal error bars in Fig. 2, were not used because of time gaps, on the order of 10-30 minutes, in either the LSM or Explorer data. These are caused by telemetry shadowing, calibration interruptions, etc.

A representative set of spectra at both Explorer and LSM for the y and z magnetic field components (tangent to the

surface) is shown in Fig. 1. The forcing spectra are seen to display the expected f^{-2} dependence characteristic of interplanetary fluctuations, while the LSM shows an f^{-1} dependence. Thus significant frequency dependent power amplification is apparent in the record.

The empirical transfer function $A_i(f)$ is defined by

$$h_{2i}(f) + h_{1i}(f) = A_i(f) h_{1i}(f) \quad , \quad (7)$$

where $h_{2i}(f)$ and $h_{1i}(f)$ are the Fourier transformed time series of the magnetic field induced in the Moon and measured on the lunar surface, and the free stream interplanetary magnetic field, respectively, and the subscript i is x , y or z . The LSM measures the sum $h_{2i}(f) + h_{1i}(f)$ while the free stream magnetic field, $h_{1i}(f)$, is measured by the Ames magnetometer on the lunar orbiting satellite, Explorer 35.

Fig. 2 shows the average ratio of power spectral densities $A_i(f)$. The mean values are the arithmetic averages using the 14 swaths of data. The error bars are the one standard deviation limits of the mean calculated from the transfer functions for the 14 time swaths. The bars do not include the error estimates in the calculation of the individual spectra. They are, however, consistent with the propagation of errors in the

individual spectra. The values of A_x lie near unity at all frequencies indicating that the interior conducting region is relatively far from the magnetometer compared to the distance to the plasma current sheath on the sunward side of the Moon. Characteristically the amplification rises from near unity for both A_y and A_z at 0.001 Hz until values near 4 are attained above about 0.02 Hz. Values of A_y are less than those of A_z over the entire frequency range. This departure increases fractionally as frequency is decreased. It is plausible that the lunar TM response is frequency dependent at frequencies above about 0.01 Hz. If so the response for the TM mode should decrease with frequency in accordance with the observation. This is the strongest evidence for contributions from both the TE and TM modes. An alternate possibility that the basic response is purely TE and that the Moon is asymmetrically excited seems less convincing but cannot be ruled out at present. We have not yet found a completely satisfactory explanation for why the northward component of the excitation is systematically higher than the eastward component. The important facts are that they both have the same slope and change in slope around 0.01 Hz. We conclude that the lunar transfer function is dominated by the TE mode with possible contributions, especially at the lower frequencies, from the TM mode.

A significant scatter appears in the amplifications A_i .

This scatter is substantially reduced by taking averages over many A_i , but is exact only if the errors have zero mean, which is approximately the case as shown in Fig. 3. A combination of all the data points $\bar{A}(f) = \left\{ \frac{1}{2} (A_y^2(f) + A_z^2(f)) \right\}^{\frac{1}{2}}$ for all frequencies up to 0.035 Hz has been made in order to investigate the distribution of the ratios of the power spectral densities. The distribution shown in Fig. 3 is a histogram of the number of cases vs. the difference of the measured value \bar{A} from the mean at each frequency, normalized by the standard deviation at that frequency and weighted by the expected error $(\bar{A}(f_0)/\bar{A}(f))$. The figure shows that the distribution is somewhat more sharply peaked than a normal one and also has a small bias.

The sources of the variations in the A_i may originate in any of several possible ways: 1) the presence of contamination especially in the Explorer data from spurious tones in the spacecraft; 2) the contribution to induction from higher order modes; 3) fluctuations in cavity currents in turn due to changing diamagnetism in the solar wind; 4) the possible contribution of TM modes to the predominantly TE spectra; 5) the possibility that some field line leakage takes place where the component of solar wind plasma pressure normal to the surface falls below the pressure of the induced magnetic field. These factors may also contribute to the droop of the average A_i at

the higher frequencies. It should be noted that there is no correlation between the A_i and sun angle, implying that field line confinement is effective for the data used here (sun angles less than 65°).

LUNAR ELECTRICAL CONDUCTIVITY PROFILE

The theory of lunar induction, discussed earlier, has been used to derive a profile of electrical conductivity from the empirical transfer function. The theoretical amplification for the lowest TE mode, computed by numerically integrating Eq. (5) with a radially dependent conductivity, is matched to the empirical transfer function using a Newton-Raphson iterative scheme. This scheme readjusts the entire conductivity profile to yield amplifications which best fit the data in a least-squares sense over the entire frequency range. This has been carried out using frequency values of 0.83, 1.7, 5, 12, 17, 22, 25 and 35 millihz. The conductivity profile is characterized by its values at the radial locations $r = 800, 1200, 1400, 1450, 1490, 1510, 1550$ and 1740 km. For $r < 800$ km the conductivity σ is set to the value at $r = 800$ km ; elsewhere a linear interpolation of $\log \sigma$ is used.

The computer calculation is started with a continuous conductivity profile defined by 8 parameters as described above. Numerical integrations are carried out to obtain

values of amplification at the eight frequencies. A comparison of these amplifications with the data provides the Newton-Raphson scheme with the input required to adjust the 8 conductivity parameters to yield a profile whose corresponding theoretical amplification curve is a better least-squares fit to the empirical transfer function. The iteration is continued until an adequate fit is obtained. The result of such a fit to the empirical amplification curve $\bar{A} = \{\frac{1}{2}(A_y^2 + A_z^2)\}^{\frac{1}{2}}$ is shown in Fig. 4. The introduction of \bar{A} permits the use of both A_y and A_z data to improve the statistics. The differences between the theoretical amplification and the empirical \bar{A} are, in our assessment, partially attributable to the various complications of the excitation process enumerated at the end of the previous section (not accounted for by the theory), as well as considerations of computer running time which limits the number of frequencies and conductivity parameters (spatial resolution) employed.

A conductivity profile is associated with the theoretical amplification curve of Fig. 4. In addition we have obtained conductivity profiles by fitting not only \bar{A} but also A_y , A_z and their one standard deviation limits. The conductivity profiles derived from the iterative least squares inversion for A_y , A_z and \bar{A} are shown in Fig. 5. The prominent spike in each conductivity profile is an invariant characteristic

of the inversions. It is centered at about $r = 1500$ km where the conductivity is nearly 10^{-2} mhos/m. The inner minimum lies at about $r = 1400$ km and the conductivity appears to rise at greater depth. Gross bounds on the conductivity profile are seen in the insert; these are determined from the one standard deviation limits of the various A's, but do not themselves represent one standard deviation limits on the conductivity profile.

The computer calculations for Figs. 4 and 5 started with a constant conductivity of 10^{-4} mhos/m. However, a number of computations have been carried out using different values for uniform starting conductivities (e.g. 10^{-3} and 10^{-5} mhos/m) and different radial locations. In every case tested, initial convergence was rapid and the final conductivity profile invariably displayed the prominent spike near $r = 1500$ km. For the profiles reported here, several values of r were chosen in the neighborhood of $r = 1500$ km to better define the conductivity spike.

Whereas the large spike in conductivity is a persistent feature of the inversions, the character of the conductivity profile at greater depth, where the conductivity appears to rise, is not so certain and our results for the conductivity at these depths must remain tentative. The surface amplifica-

tion is a rather insensitive function of core conductivity because of the relatively small core volume and the distance to the surface.

Figure 6 shows the manner in which the amplitude and phase of the relative field strength vary with depth in the Moon, indicating different degrees of field compression at various frequencies. The conductivity profile used in this calculation was the one associated with the theoretical fit of \bar{A} (see Fig. 5). In the range $r = 1500$ to 1740 km, the field is essentially constant and phase shift is small, consistent with the low conductivity (large skin depth) in this region. The large rise in conductivity at $r = 1500$ km produces a penetration barrier (small skin depth) for the higher frequencies. Below this barrier the high frequency variations in the field are low in amplitude and have large phase shifts. Over the high frequency range the barrier essentially confines field lines to the outer region, producing a nearly constant amplification with frequency, consistent with the data. For the lower frequencies the barrier is not effective and the relatively low conductivity in the range $r < 1500$ km allows the field to penetrate to the deep interior, yielding a smaller amplification. Where phase shifts are greater than 90 deg the field lines connected with the driving field have been excluded; the resulting compression leads to the

amplification.

COMPARISON WITH OTHER CONDUCTIVITY PROFILES

A physical understanding of the appearance of the large conductivity spike can be obtained as follows. In a two layer model with an infinitely conducting core and a non-conducting shell the amplification of the tangential magnetic field components is given by

$$1 + \frac{3}{2} \frac{(\text{core volume})}{(\text{shell volume})}$$

This simple result requires that the high frequency skin depth barrier be near $r = 1500$ km for an amplification ≈ 4 . At frequencies above 0.02 Hz essentially no wave penetration takes place through this barrier. Thus the volume available in the core for field lines is insignificant compared to that in the nonconducting shell. This means that the amplification becomes independent of frequency, i.e. $dA/df \rightarrow 0$ at high frequency. Concurrent with the high frequency limitation is the requirement that A drop to near unity at the lower frequencies. If it were assumed that the electrical conductivity were monotonic, so that the interior conductivity were uniformly high, then the low frequency amplification would be in excess of the observed values.

The inadequacies of monotonic conductivity profiles are shown in Fig. 7. The experimental r.m.s. amplification data \bar{A} (circled points with associated error bars) can be compared with the amplification curve for the \bar{A} conductivity profile of Fig. 5 (labelled "best fit") and amplification curves of several monotonic conductivity profiles. The "2 layer" amplification curve was calculated for a model with a core of radius of 1560 km and a constant conductivity of 7.6×10^{-4} mhos/m, and a shell of zero conductivity. This value of the core conductivity provides a best fit to the experimental \bar{A} for the given core radius. Other best fit two layer models with different core radii have been investigated; the one used in Fig. 7 yields an amplification curve which matches the data most closely. The amplification curve labelled DYAL and PARKIN (1971) was computed from a 3 layer conductivity model proposed by these authors. The parameters of their model are $\sigma = 10^{-2}$ mhos/m for $0 < r < 1044$ km, $\sigma = 1.7 \times 10^{-4}$ mhos/m for $1044 \text{ km} < r < 1653$ km and $\sigma = 0$ in the outer shell. In other 3 layer conductivity models consistent with the data analysis of DYAL and PARKIN (1971), the outer boundary of the region of intermediate conductivity can be located anywhere between $r = 1653$ and 1740 km. We have computed the amplification curves for a number of these additional 3 layer models; none provide a better fit to the observational curve. Also shown in Fig. 7 are amplification curves from conductivity profiles proposed

by SILL (1971) (model 3 in that paper) and NESS (1969). Other conductivity models investigated by SILL (1971) fit the experimental data no better than his model 3. The conductivity model of NESS (1969) consists of a core of radius 1426 km with $\sigma = 8 \times 10^{-5}$ mhos/m, and a nonconducting shell. Amplification curves from conductivity models of WARD (1969) were also considered but these were rejected upon comparison with the observational data.

The "2 layer" amplification curve shown in Fig. 7 is, compared to the experimental data, high at $f < 0.0035$ Hz and $f > 0.03$ Hz, and low in the range $0.01 \text{ Hz} < f < 0.02 \text{ Hz}$. The data show a flat response at frequencies above 0.02 Hz, whereas the slope of the "2 layer" curve is high at these frequencies. Furthermore as the frequency increases the curvature of the data changes from positive to negative at about 0.003 Hz. The "2 layer" amplification curve is everywhere concave up. This "s" shaped character of the experimental data is faithfully reproduced only by our "best fit" conductivity profile. Further work is in progress to improve the high frequency slope of our "best fit" model. This will probably lead both to a higher value of the maximum conductivity and a steeper slope of the conductivity profile at the outer edge, effects which will tend to sharpen the conductivity spike in order to allow penetration of low frequency magnetic field fluctuations.

COMPOSITIONAL AND THERMAL MODEL

The electrical conductivity profile cannot be explained by a uniform material and a plausible thermal profile. In the region from the surface to $r = 1500$ km where the conductivity attains its maximum value, the rise of conductivity with depth is a reasonable consequence of the accompanying increase of temperature in a material of uniform composition. Below $r = 1400$ km the apparent rise in conductivity is again explainable by an increase in temperature. On the other hand the precipitous decrease of electrical conductivity by 2 to 3 orders between $r = 1500$ and 1400 km cannot be explained as due to temperature. Either a compositional change, phase change, or a combination of the two is required. Thus a reasonable model for stratification of the Moon, limited by the present poor spatial resolution of the analysis indicates a core out to $r \approx 1400$ km overlain by a mantle of higher conductivity material, plus possibly a transition layer at $r = 1400 - 1500$ km.

In order to infer a temperature profile from the conductivity profile it is necessary to use conductivity-temperature functions of known rock materials. The Apollo basalts (SCHWERER et al., 1970; NAGATA et al., 1970) are representative of the most conducting rocky matter known. On the other hand olivine (dunite) or olivine-peridotite (ENGLAND et al., 1968)

is representative of poorly conducting geological material. The peak conductivity value found in the lunar mantle corresponds to a temperature of about 450°C for lunar basalt or 950°C for olivine. Since the temperature just under the lunar surface is -30°C , the corresponding thermal gradients in the outer mantle are about 2°K/km and 4°K/km .

The precipitous decrease in electrical conductivity of $10^2 - 10^3$ as depth increases from 250 km to 350 km takes place in a distance where the temperature rises at least 100 degrees. While the absolute conductivities of the materials are unsure because of impurities, etc., it seems clear that the change in conductivity around 300 km depth requires a change in composition. Thus one model fitting the data has an olivine-like core, possibly a lower mantle composed of a material transitional between the substrate and the upper mantle, and an upper mantle having the conductivity of Apollo basalt (see Fig. 8). Since the present frequency resolution is insufficient to estimate the conductivity close to the surface, these results do not preclude the presence of an anorthositic crust (WOOD et al., 1970). The volume of the mantle comprises about one half the total volume of the Moon. To fill it completely with a basaltic extract is in conflict with geochemical constraints which imply at most a 10-15% contribution by volume. The upper mantle may have to be composed only partly of a basalt-like

substance to account for the apparent dependence of the upper mantle conductivity upon temperature. The actual basalt-like thickness cannot be assayed yet because of limited spatial resolution. An alternative model which avoids the difficulty of finding a source of so much basalt has a layer of iron concentration at $r = 1400$ to 1500 km, such as could occur from a differentiation of the outer 340 km (WOOD et al., 1970; cf. UREY et al., 1971).

For our compositional model the temperature at $r = 1500$ km is 450°C and the average near surface thermal gradient is 2°K/km . The temperature at $r = 800$ km, computed from the conductivity profiles shown in Fig. 5 together with an olivine conductivity function is in the range $750\text{-}800^{\circ}\text{C}$, decreasing to approximately 550°C at 1400 km where the local minimum in electrical conductivity is observed. A calculation based upon more conducting matter would depress the computed temperatures. R. REYNOLDS (private communication) has shown that after 4.5 billion years a nonconvecting Moon of 25% ordinary chondritic radioactive composition and an initial uniform temperature of 0°C attains a near surface thermal gradient of approximately 2°K/km and a uniform core temperature of about 800°C . Hence a thermal model consistent with the conductivity requires appreciable depletion of the heat sources in the Moon relative to ordinary chondrites.

An approximate value for the lunar heat flux can be calculated from the near surface gradient determined above. For silicate material the thermal conductivity is 0.008 cal/cm sec deg though it is known that it will decrease with increasing temperature (HORAI et al., 1970; MURASE and McBIRNEY, 1970). This effect will not introduce a substantial error in the estimate of the heat flux which we find to be 1.6×10^{-7} cal/cm² sec using the "basalt" composition for the mantle; olivine would double this estimate. The former value is approximately 1/8 that of the Pre-Cambrian regions of Earth (KAULA, 1968). For a Moon scaled Earth, the flux would be twice that actually measured for a "basalt" model and approximately equal for an olivine model.

We wish to thank our colleagues C.W. Snyder, M. Neugebauer, J.H. Wolfe, and the Vela group at Los Alamos Scientific Laboratory for supplying plasma data for testing the field line confinement problem. Constructive comments by W.M. Kaula have substantially improved this paper.

APPENDIX

The spherical harmonic expansions for the potential and magnetic field of the transverse electric part of the solar wind excitation are

$$\Omega = \mu v H_0 \frac{\sin \varphi}{r} \sum_{\ell=1}^{\infty} \beta_{\ell} r j_{\ell} \left(\frac{2\pi r}{\lambda} \right) P_{\ell}^1 (\cos \theta) ,$$

$$\begin{Bmatrix} H_{\theta} \\ H_{\varphi} \end{Bmatrix} = H_0 \begin{Bmatrix} \sin \varphi \\ \cos \varphi \end{Bmatrix} \sum_{\ell=1}^{\infty} \beta_{\ell} \frac{\lambda}{2\pi i r} \frac{d}{dr} \left(r j_{\ell} \left(\frac{2\pi r}{\lambda} \right) \right) \begin{Bmatrix} \frac{dP_{\ell}^1(\cos \theta)}{d\theta} \\ \frac{P_{\ell}^1(\cos \theta)}{\sin \theta} \end{Bmatrix}$$

$$H_r = H_0 \sin \varphi \sum_{\ell=1}^{\infty} \beta_{\ell} \frac{\lambda}{2\pi i r} \ell(\ell+1) j_{\ell} \left(\frac{2\pi r}{\lambda} \right) P_{\ell}^1 (\cos \theta) .$$

The TE part of the magnetic field is related to the TE potential by

$$H_r = - \frac{i}{\mu \omega} \left(\frac{\partial^2}{\partial r^2} + k^2 \right) (r\Omega) , \quad H_{\theta} = - \frac{i}{\mu \omega r} \frac{\partial}{\partial r} \left(r \frac{\partial \Omega}{\partial \theta} \right) ,$$

$$H_{\varphi} = \frac{-i}{\mu \omega r \sin \theta} \frac{\partial}{\partial r} \left(r \frac{\partial \Omega}{\partial \varphi} \right)$$

Thus the TE magnetic field in the lunar interior is

$$\begin{Bmatrix} H_{\theta} \\ H_{\varphi} \end{Bmatrix} = H_0 \begin{Bmatrix} \sin\varphi \\ \cos\varphi \end{Bmatrix} \sum_{\ell=1}^{\infty} \beta_{\ell} \frac{\lambda a}{2\pi i r} \frac{dG_{\ell}}{dr} \left\{ \begin{array}{c} \frac{dp_{\ell}^1(\cos\theta)}{d\theta} \\ \frac{p_{\ell}^1(\cos\theta)}{\sin\theta} \end{array} \right\} ,$$

$$H_r = H_0 \sin\varphi \sum_{\ell=1}^{\infty} \beta_{\ell} \ell(\ell+1) \frac{\lambda a}{2\pi i r} \left(\frac{G_{\ell}}{r} \right) p_{\ell}^1(\cos\theta) .$$

REFERENCES

- BENDAT J.S. and PIERSON A.G. (1966) Measurement and Analysis of Random Data. John Wiley.
- BLANK J.L. and SILL W.R. (1969) Response of the Moon to the time-varying interplanetary magnetic field. J. Geophys. Res. **74**, 736-743.
- COLBURN D.S. and SONETT C.P. (1966) Discontinuities in the solar wind. Space Science Rev. **5**, 439-506.
- DYAL P., PARKIN C.W. and SONETT C.P. (1970) Lunar surface magnetometer experiment. NASA SP-235.
- DYAL P. and PARKIN C.W. (1971) Electrical conductivity and temperature of the lunar interior from magnetic transient-response measurements. Submitted to Proc. Apollo 12 Lunar Science Conf., Geochim. Cosmochim. Acta.
- ENGLAND A.W., SIMMONS G. and STRANGWAY D. (1968) Electrical conductivity of the Moon. J. Geophys. Res. **73**, 3219-3226.
- HORAI K., SIMMONS G., KANAMORI H. and WONES D. (1970) Thermal diffusivity, conductivity and thermal inertia of Apollo 11 lunar material. Proc. Apollo 11 Lunar Science Conf., Geochim. Cosmochim. Acta Suppl. 1, Vol. 3, pp. 2243-2249.
- JENKINS G.W. and WATTS D.G. (1968) Spectral Analysis and its Applications. Holden-Day.
- JOHNSON F.S. and MIDGLEY J.E. (1968) Notes on the lunar magnetosphere. J. Geophys. Res. **73**, 1523-1532.

- KAULA W.M. (1968) An Introduction to Planetary Physics. John Wiley.
- LAHIRI B.N. and PRICE A.T. (1939) Electromagnetic induction in non-uniform conductors, and the determination of the conductivity of the Earth from terrestrial magnetic variations. Phil. Trans. R. Soc. A237, 509-540.
- MIHALOV J.D., COLBURN D.S., CURRIE R.G. and SONETT C.P. (1968) Configuration and reconnection of the geomagnetic tail. J. Geophys. Res. 73, 943-959.
- MURASE T. and MCBIRNEY A.R. (1970) Thermal conductivity of lunar and terrestrial igneous rocks in their melting range. Science 170, 165-167.
- NAGATA T., RIKITAKE T. and KONO M. (1970) Electrical conductivity and the age of the Moon. Presented at the Thirteenth Plenary Meeting, COSPAR, Leningrad, USSR.
- NESS N.F. (1969) The electrical conductivity and internal temperature of the Moon. Goddard Space Flight Center Report X-616-69-191 (also presented as paper K11 at XIIth COSPAR, Prague, May, 1969).
- SCHUBERT G. and SCHWARTZ K. (1969) A theory for the interpretation of lunar surface magnetometer data. The Moon 1, 106-117.
- SCHWERER F.C., NAGATA T. and FISHER R.M. (1971) Electrical conductivity of lunar rock and chondritic meteorites. Submitted to The Moon.

- SILL W.R. (1971) Electrical conductivity and temperature of the lunar interior. J. Geophys. Res. 76, 251-256.
- SONETT C.P. (1966) Modulation and sampling of hydromagnetic radiation. Space Research VI, Spartan Books, (editor R.L. Smith-Rose) 280-322.
- SONETT C.P. and COLBURN D.S. (1968) The principle of solar wind induced planetary dynamos. Phys. Earth and Plan. Int. 1, 326-346.
- SONETT C.P., SMITH B.F., COLBURN D.S., SCHUBERT G. and SCHWARTZ K. (1971a) The lunar electrical conductivity profile: mantle-core stratification, near surface thermal gradient, heat flux and composition. Nature, in press.
- SONETT C.P., DYAL P., PARKIN C.W., COLBURN D.S., MIHALOV J.D. and SMITH B.F. (1971b) Whole body response of the Moon to electromagnetic induction by the solar wind, Science, (in press).
- SONETT C.P., DYAL P., COLBURN D.S., SMITH B.F., SCHUBERT G., SCHWARTZ K., MIHALOV, J.D. and PARKIN C.W. (1971c) Induced and permanent magnetism on the Moon: structural and evolutionary implications. Presented at the 14th General Assembly I.A.U. (to appear in Highlights of Astronomy 1970, ed. C. de Jager, D. Reidel).
- UREY H.C., MARTI K., HAWKINS J.W. and LIU M.K. (1971) Model history of the lunar surface (preprint).
- WARD S.H. (1969) Gross estimates of the conductivity, dielectric constant, and magnetic permeability distributions in the Moon. Radio Science 4, 117-137.

WOOD J.A., DICKEY J.S., MARVIN U.B. and POWELL B.J. (1970)
Lunar anorthosites and a geophysical model of the Moon.
Proc. Apollo 11 Lunar Science Conf., Geochim Cosmochim.
Acta Suppl. 1, Vol. 1, pp 965-988.

FIGURE CAPTIONS

- Fig. 1 Power spectral density determinations for simultaneous magnetic field observations on the lunar surface (Apollo 12) and in the solar wind near the Moon (Explorer 35). The y component is east and the z component north at the Apollo 12 site. Significant amplification is observed, increasing with frequency. Length of the time series is 2 hours.
- Fig. 2 Amplitude of the transfer function (ratio of lunar surface to free stream magnetic measurements) vs. frequency. The error bars for frequency are the windows defined by the lags in the autocorrelation calculation. The error bars in amplification are the one standard deviation limits determined from the means of 14 data spectra. Strong amplification is observed in the tangential (north and east) components of the field, while for the normal component the amplification follows the expected value of unity.
- Fig. 3 Distribution of the values of the differences of $\bar{A}(f)$ from the mean \bar{A} at each frequency for all frequencies up to 0.035 Hz in units of the normalized standard deviation.

Fig. 4 The rms tangential lunar transfer function, $\bar{A} = [0.5(A_y^2 + A_z^2)]^{\frac{1}{2}}$ and the normal transfer function A_x as a function of frequency. The error bars, frequency windows, and directions are as shown in Fig. 2. The solid line is the value of amplification calculated from the conductivity profile whose corresponding amplification is fitted to experimental values at frequencies of 0.83, 1.7, 5, 12, 17, 22, 25, and 35 millihz.

Fig. 5 Lunar bulk electrical conductivity profiles determined from the individual transfer functions A_y , A_z , and \bar{A} . The prominent rise of σ from the surface inwards to $r = 1500$ km is apparent for all three cases as well as the subsequent decrease inwards to $r = 1400$ km followed by a more gradual rise. A tentative version of a lunar thermal profile is shown as the grey overlay with temperatures indicated on the right hand margin. This profile is a fit of conductivities to a Nagata basalt in the mantle, an England olivine in the core, and the known subsurface temperature of -30°C . The insert is shown to suggest extreme values of the σ 's using the one standard deviation limits of the A 's to calculate conductivities.

Fig. 6 Profiles of magnetic field amplitude and phase for the conductivity profile labelled \bar{A} in Fig. 5. The values are normalized to the transfer function at the lunar surface. The region of high conductivity centered at $r = 1500$ km (see Fig. 5) is responsible for strong attenuation and large phase shift at the higher frequencies. There is a correspondence between the selective attenuation shown here and the amplification vs. frequency curve of Fig. 4, as discussed in the text. Negative phase angle in this figure represents a time delay with respect to the driving function.

Fig. 7 The experimental r.m.s. tangential lunar transfer function, \bar{A} , as a function of frequency. The error bars are the same as those in Figs. 2 and 4. The curve labelled "best fit" are the values of the amplification for the conductivity profile labelled \bar{A} in Fig. 5. The "2 layer" curve was calculated for a model with a core of radius 1560 km and a constant conductivity of 7.6×10^{-4} mhos/m, and a shell of zero conductivity. This value of the core conductivity provides a best fit to \bar{A} for the given core radius. The DYAL and PARKIN (1971) amplification curve was calculated for a model with an inner core of radius 1044 km and a conductivity of 10^{-2} mhos/meter, a middle layer extending to 1653 km with a conductivity

of 1.7×10^{-4} mhos/m and an outer layer of zero conductivity. Other amplification curves are based on conductivity models proposed by NESS (1969) and SILL (1971). Note that the "2 layer" curve does not duplicate the "S" nature of the experimental data.

Fig. 8 Model Moon based upon the magnetometer data, the derived conductivity profiles, and the consistent fit of σ to rocky material. The anorthositic crust is taken from WOOD et al. (1970); it is not seen in the present analysis.

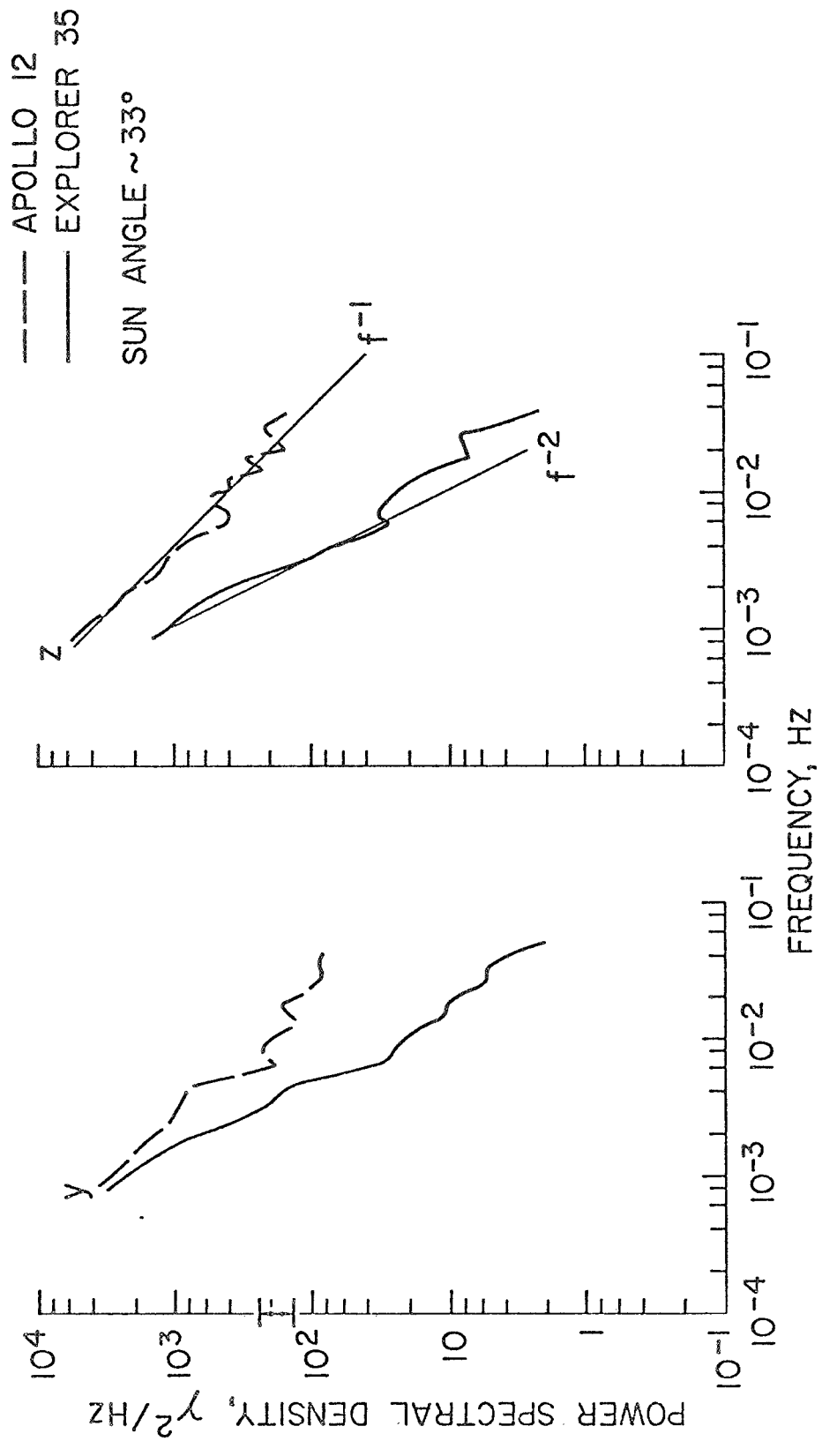


Figure 1

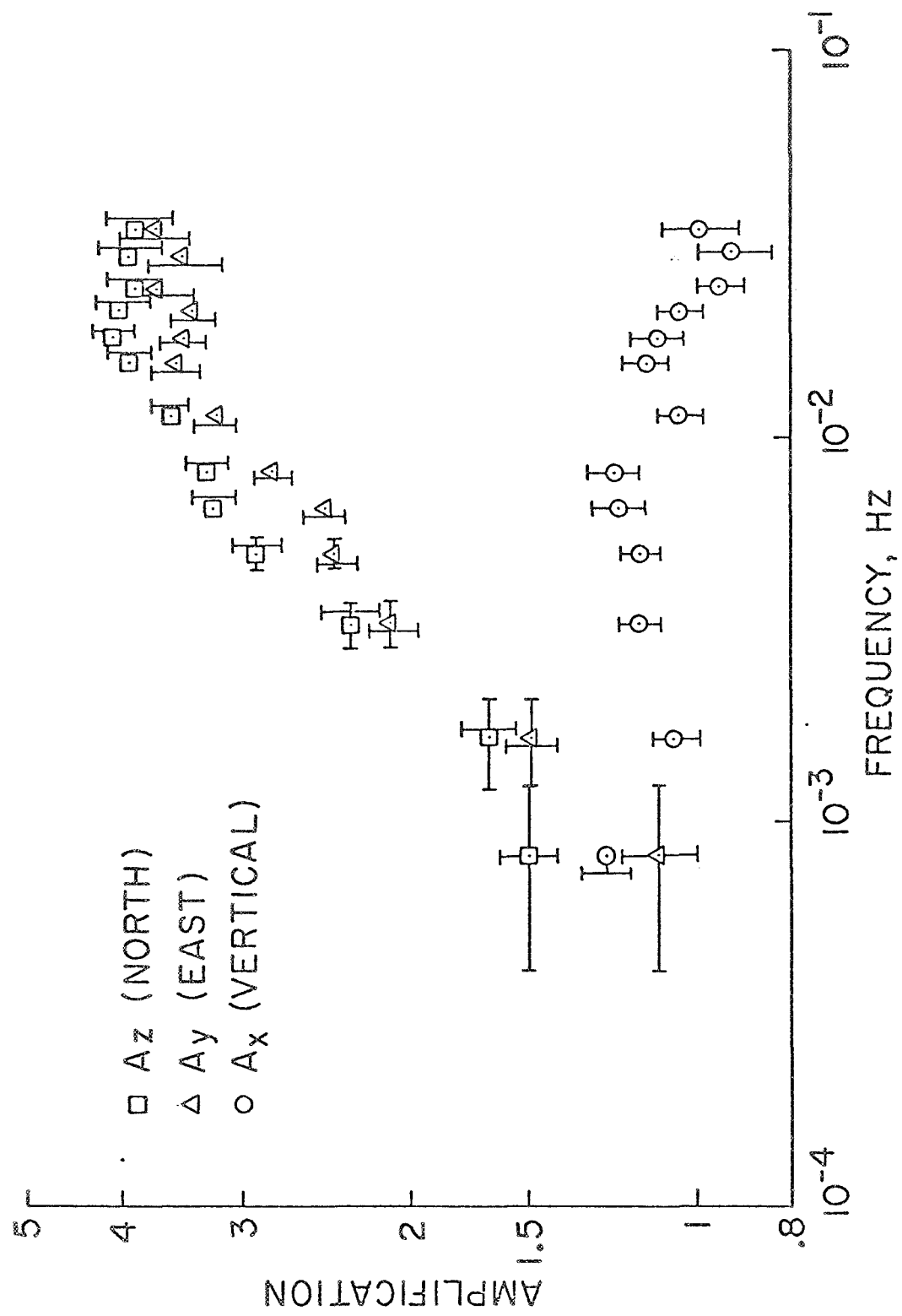


Figure 2

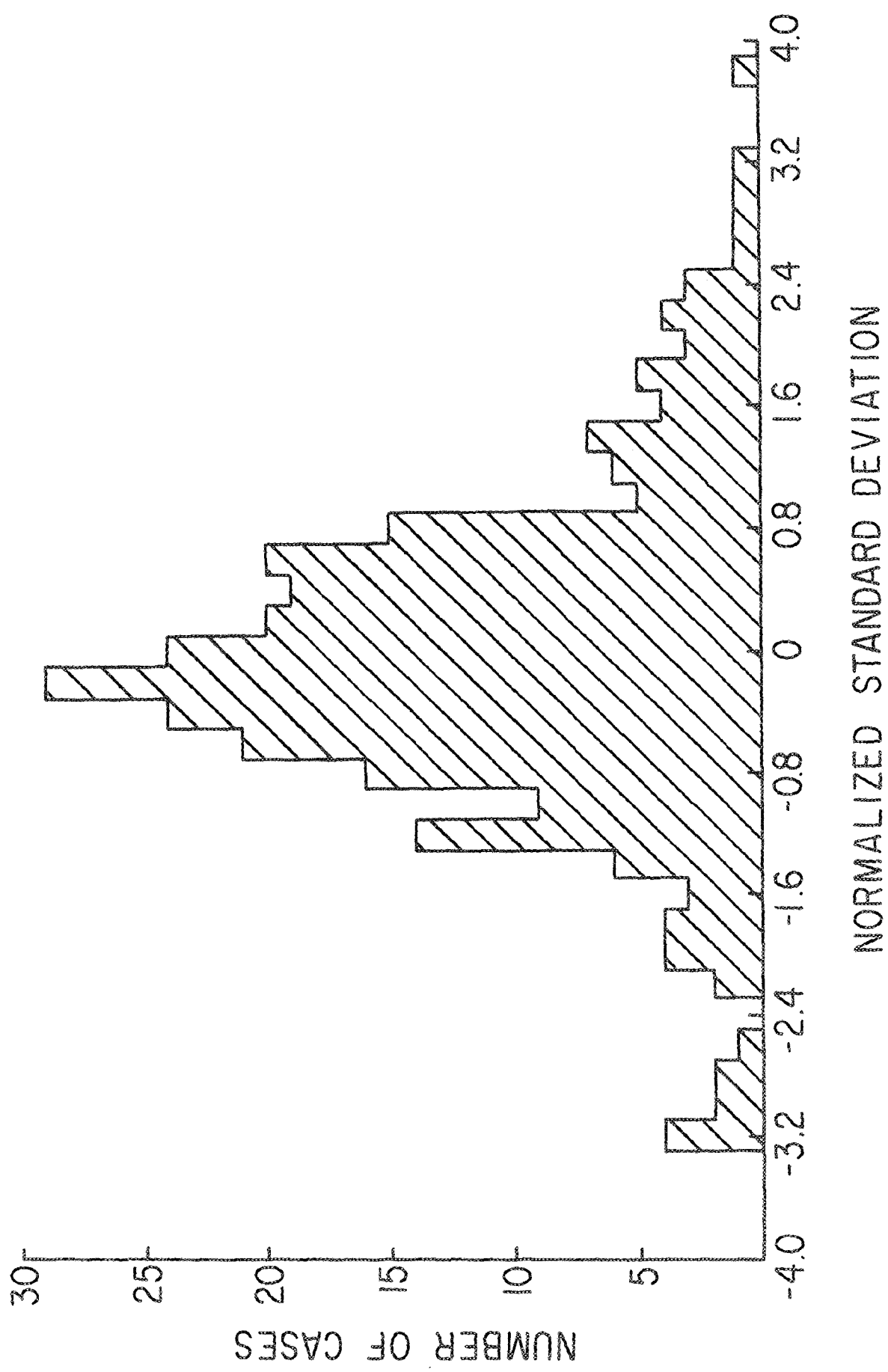


Figure 3

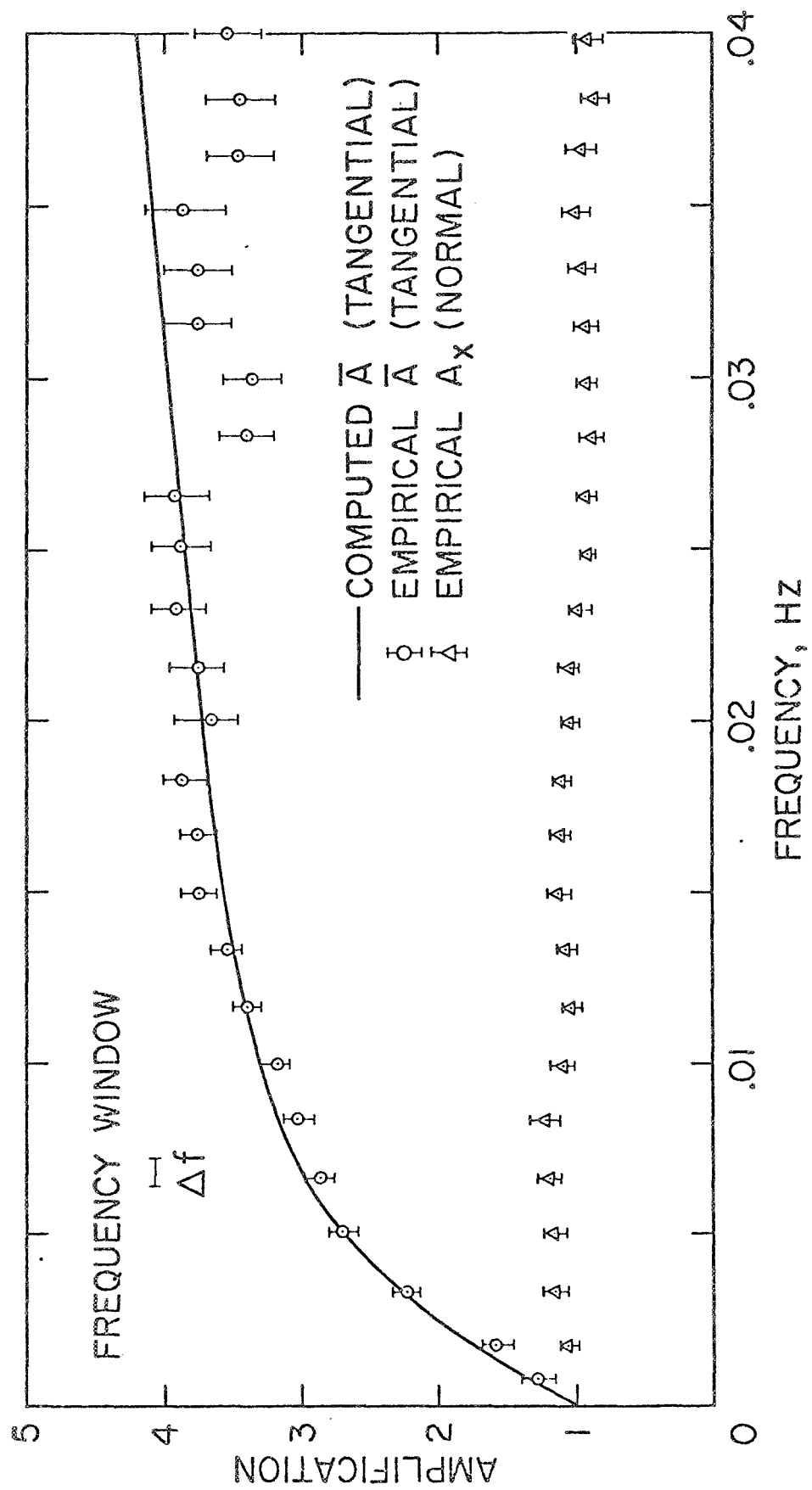


Figure 4

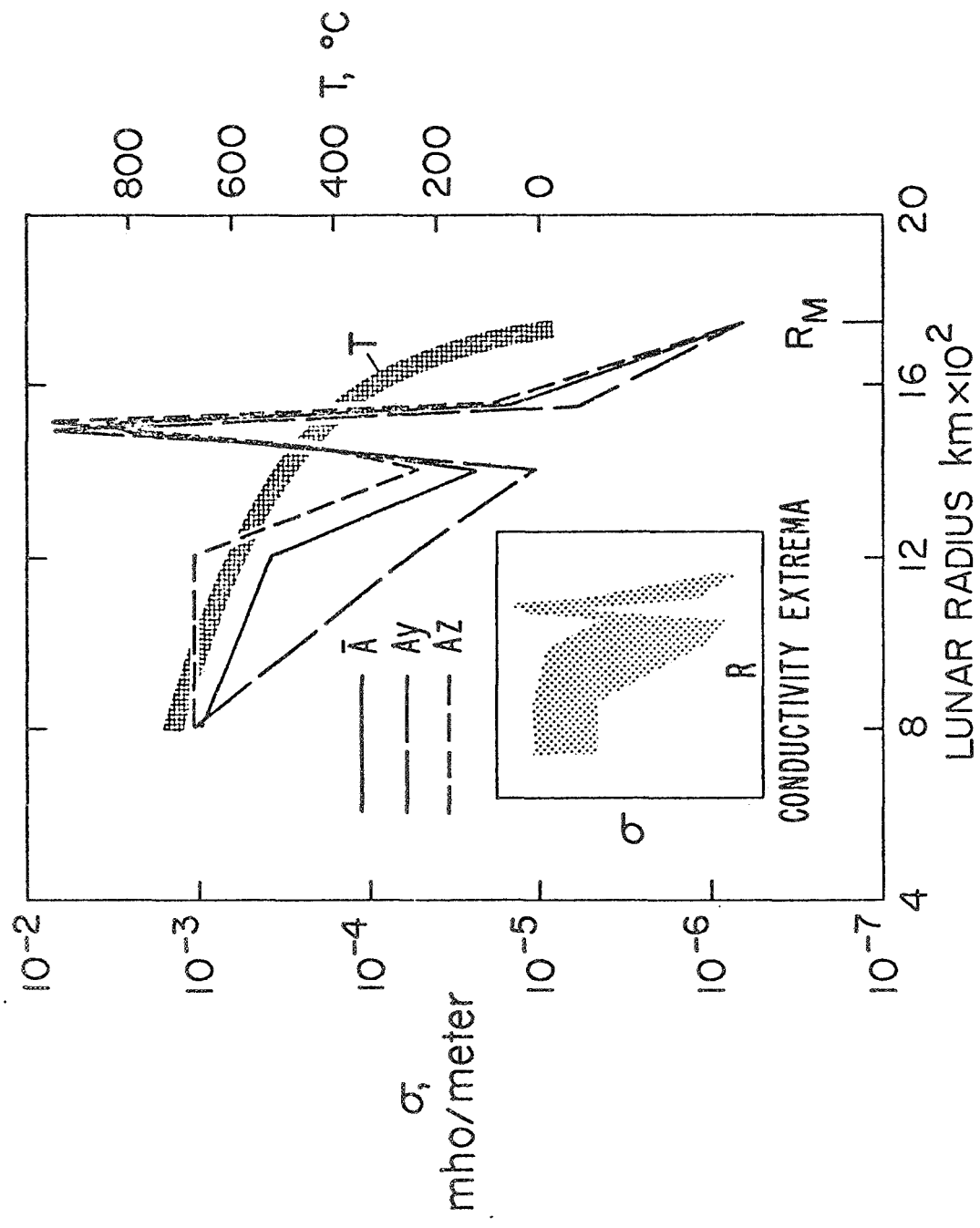


Figure 5

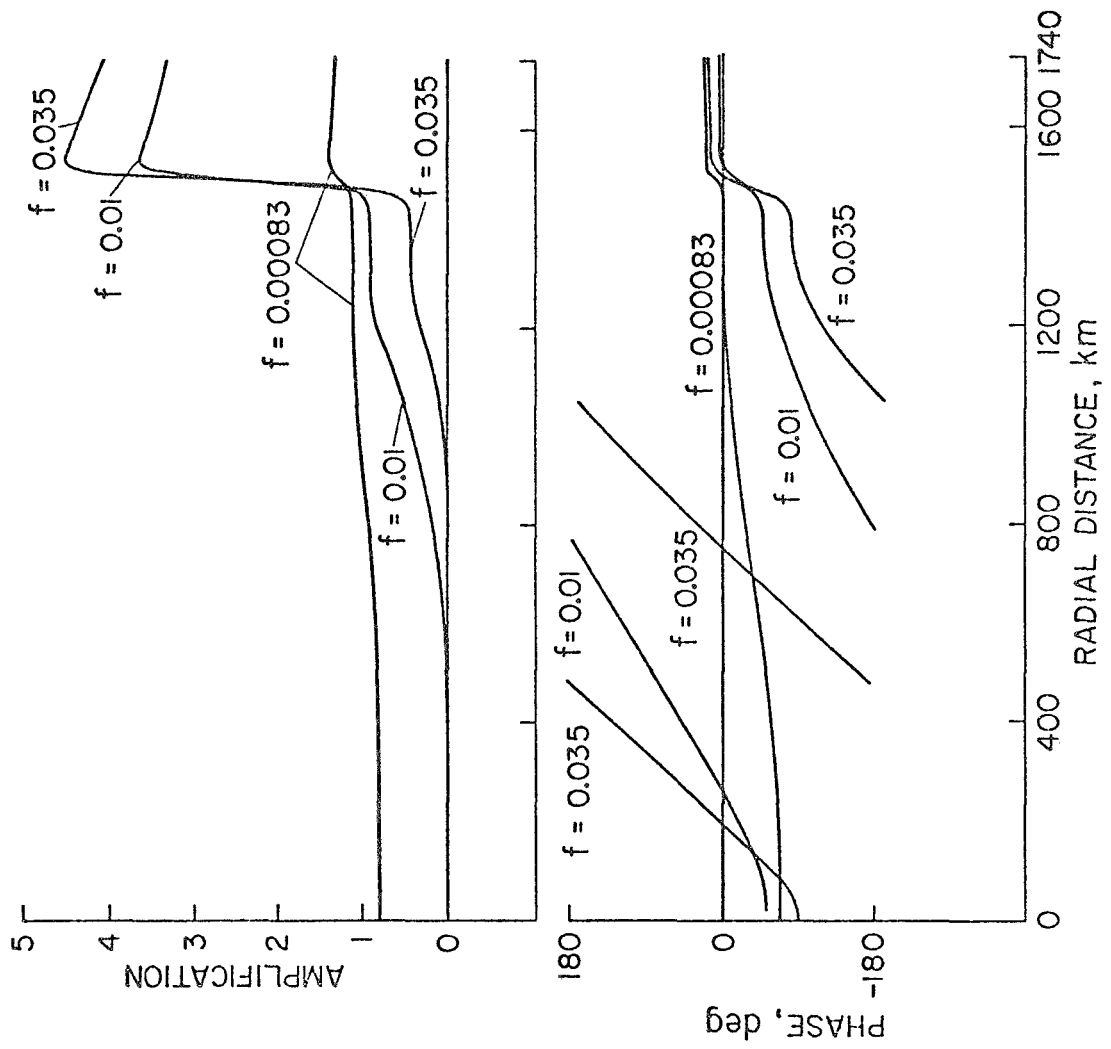


Figure 6

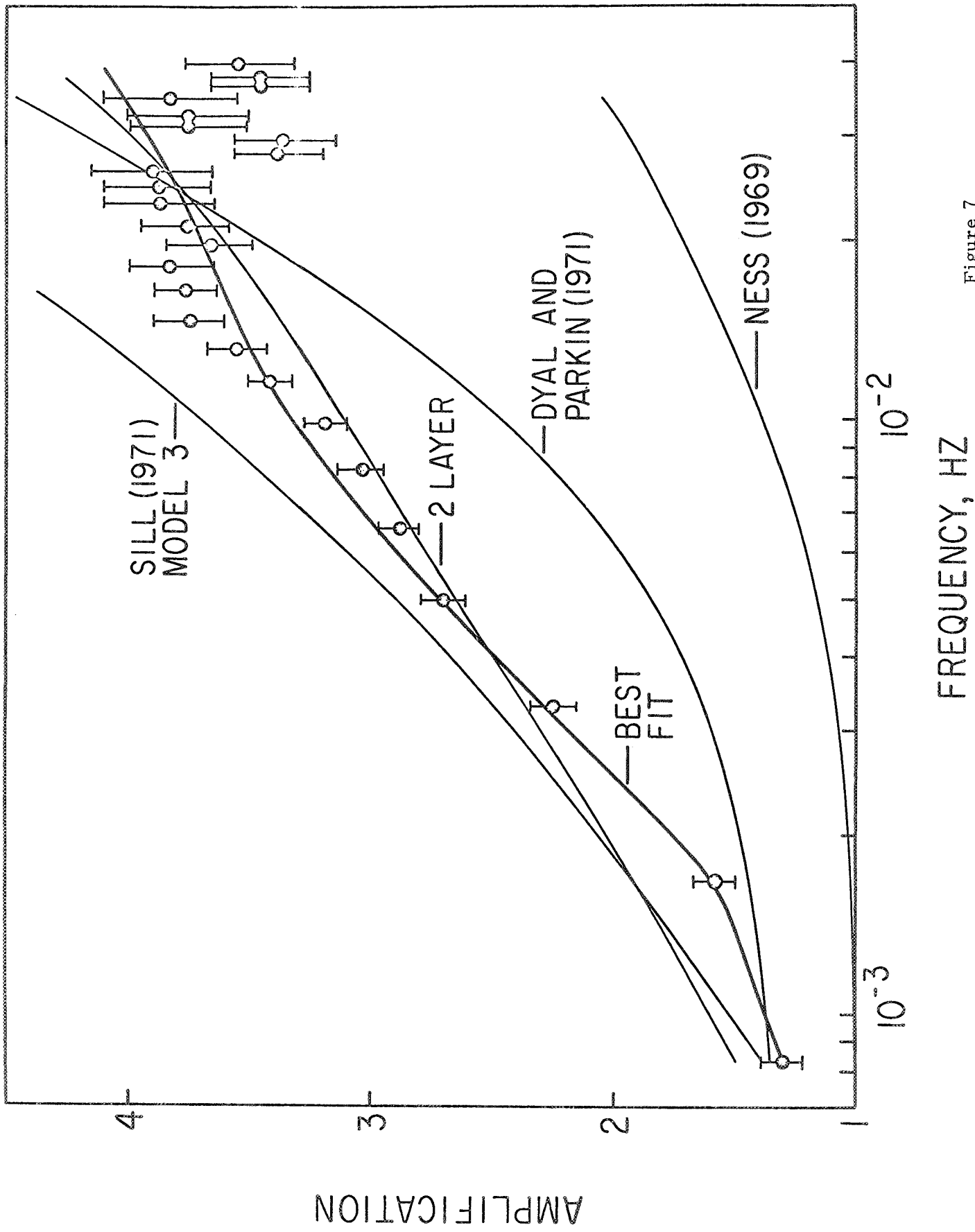


Figure 7

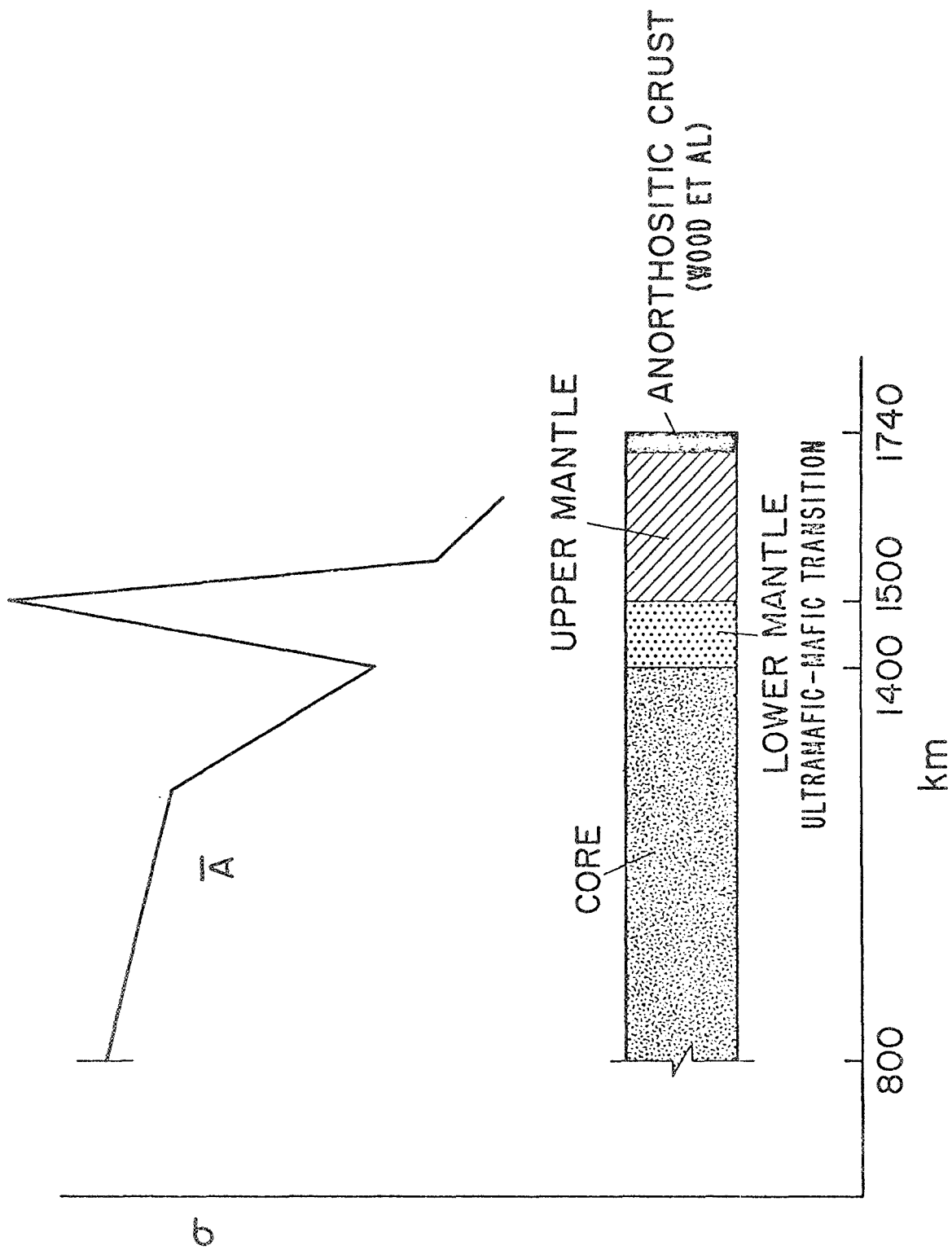


Figure 8